Femtosecond extreme ultraviolet spectroscopy of an iridium photocatalyst reveals oxidation state and ligand field specific dynamics.

Clare A. Leahy[1] and Josh Vura-Weis[1*]

[1] Department of Chemistry, University of Illinois at Urbana-Champaign, Urbana, IL

ABSTRACT: Femtosecond X-ray absorption spectroscopy at the Ir O_3-edge and $N_{6,7}$-edges is performed on the photocatalyst iridium(III) tris(2-phenylpyridine), Ir(III)$(ppy)_3$ using a tabletop high-harmonic source. Extreme ultraviolet (XUV) absorption between 44 eV and 72 eV measures transitions from the Ir $5p_{3/2}$ and $4f_{5/2,7/2}$ core to 5*d* valence orbitals, and the position of these spectral features is shown to be sensitive to the oxidation state and ligand field of the metal center. Upon excitation of the singlet metal-to-ligand charge transfer (^{1}MLCT) band at 400 nm, a shift in the spectra due to the formation of the Ir(IV) center is observed, as is the creation of a new spectral feature corresponding to transitions into the t_{2g} hole. Vibrational cooling of the MLCT state on the 3 ps and 16 ps timescales is measured as changes in the intensity of the transient features. This work establishes XUV spectroscopy as a useful tool for measuring the electronic structure of 3rd row transition metal photosensitizers and catalysts at ultrafast timescales.

Introduction

Table-top extreme ultraviolet (XUV) spectroscopy in the 40-100 eV energy range has been shown to be a powerful technique for probing the ultrafast photophysics of 1st row transition metal coordination complexes.[1–10] The $M_{2,3}$-edge, corresponding to 3p → 3d transitions, is sensitive to oxidation state, ligand field, and spin-state, providing direct insight into key changes at the metal center.[9] This technique has been used to examine excited state dynamics at various 1st row transition metal centers, such as nickel,[2,4,6,11] iron,[2,7,8,12–14] & cobalt,[4,5,15,16] for photocatalysts and other molecular systems.

Far less attention has been paid to the potential for XUV spectroscopy of 3rd-row metals. This energy range contains the $O_{2,3}$- and $N_{6,7}$-edges of 5d metals: the $O_{2,3}$-edges corresponds to $5p_{1/2,3/2}$ to valence orbital transitions, while the $N_{6,7}$-edges corresponds to $4f_{5/2,7/2}$ to valence orbital transitions. Prior work has generally been limited to metallic samples or atomic vapors of 3rd row transition metals in the XUV region. Sonntag, Kunz, and coworkers first performed systematic acquisition of the 40-200 eV region for metallic 2nd and 3rd row transition metals in the 1960s, observing the suite of edges that included proposed $O_{2,3}$- and $N_{6,7}$-edges between 40-120 eV for tungsten through gold.[17] Later studies using the dual laser-produced plasma technique more closely examined plasmonic vapors of platinum and tungsten identifying specific transitions and interactions observed for the $O_{2,3}$ and $N_{6,7}$-edges and examining correlation and relativistic effects.[18,19] More recent work has examined the photoabsorption spectra of gold,[20] iridium,[21] and other 3rd row metals[22] in the XUV region towards calculating and fitting the transitions, finding the edges were dominated by a great number of lines from 4f-to-[5d,6s] and 5p-to-[5d,6s] transitions. Leone and coworkers recently used transient XUV to examine carrier dynamics in WS_2 at the tungsten O_3- and $N_{6,7}$-edges.[23] However, to our knowledge the spectroscopy of molecular 5d coordination complexes in this energy region is completely unexplored.

In this work, we develop an understanding of excited state dynamics at the O_3- and $N_{6,7}$-edges of 3rd row transition metal coordination complexes, specifically with iridium(III) centers, using XUV spectroscopy. Cyclometalated iridium(III) complexes are ubiquitous photocatalysts and sensitizers, with wide use in photoredox chemistry.[24–32] They are also common dopants in organic light-emitting diodes (OLEDs).[33–35] These complexes generally have strong molar absorptivity (~10,000 $M^{-1}cm^{-1}$) in the UV-Vis spectral region, allowing for excitation at accessible single wavelengths or ambient light sources.[26,33,34,36–42] Common ligand scaffolds, such as bipyridine (bpy) and 2-phenylpyridine (ppy), are modifiable through ligand exchange or substitutions at select positions, allowing for easy tuning of the charge transfer bands and dynamics.[29,30,37,41] Their excited state redox potentials are well-suited for transferring electrons in a variety of transformations.[28,41,43–45] Finally, these triplet states are generally long-lived (ns-μs) due to the forbidden transition to return to the singlet ground state, allowing for sufficient time to transfer the energy into the desired process.[45–47] The strong spin-orbit couplings (SOC) of iridium facilitates efficient intersystem crossing (ISC) between singlet and triplet states, which give high quantum emission yields from the triplet state.

In this work, we performed transient O_3- & $N_{6,7}$-edge XANES on Ir(III)$(ppy)_3$, showing that metal-based photodynamics can be tracked at this edge akin to synchrotron-based transient $L_{2,3}$-edge XANES. The ^{3}MLCT excited state is clearly identified by the appearance of a new core-to-valence 5d t_{2g} transition and a blue shift in the core-to-valence 5d e_g transition. This result provides a foundation for future studies examining the photochemistry of late 3rd row coordination complexes using XUV spectroscopy.

Methods

Iridium(III) tris(2-pheynylpyridine) (Ir(III)$(ppy)_3$) and sodium hexachloroiridate(III) ($Na_3Ir(III)Cl_6$) were purchased from Sigma Aldrich. Thin film samples were prepared through sublimation using a house-build thermal evaporator or dropcast onto 50 or 100 nm Si_3N_4 substrate; specific details are given below. Static UV-Vis spectra were

acquired to confirm sample identity and to check for degradation pre- and post-experiments. Ir(III)(ppy)$_3$ samples (~114 nm thickness) were deposited onto 50 and 100 nm Si_3N_4 membranes using thermal evaporation (or on glass for the UV/Visible spectrum) and stored in the dark underneath dinitrogen atmosphere in a drybox. $Na_3Ir(III)Cl_6$ samples were prepared by taking a concentrated, filtered solution of the target complex in dimethylformamide (DMF) and drop-casting onto 100 nm Si_3N_4 membranes.

The tabletop XUV probe was generated through the process of high-harmonic generation (HHG) as described in prior work.[13] In brief, the 1 kHz, 35 fs, 800 nm pulse of a NIR driving laser is focused into a semi-infinite gas cell containing approximately 100 Torr of neon or 50 Torr of argon gas to generate approximately 20 fs XUV pulses in the energy range from 55-80 eV or 35-60 eV, respectively. The residual NIR pulses were filtered using a 100 nm (Ne) or 200 nm (Ar) thick Al foil and creating a flux of ~10^5 photons per pulse per 0.1 eV at 64.7 eV (Ne) or 53.5 (Ar) at the sample position. The spectrometer resolution is measured using the absorption lines of Kr^+ and Xe^+ and averaged ~0.4 eV (Ne) and 0.33 eV (Ar) FWHM for these experiments. A secondary output from the same laser source was sent through an α-BBO crystal to generate the 400 nm, ~50 fs pump pulse via second harmonic generation. Transient absorption of a thin film of α-Fe_2O_3 is used to determine time zero (t_o) and the instrument response function (IRF) of 90 fs FWHM for Ne conditions, while PbI_2 was used for Ar conditions to determine t_o and the IRF of 123 fs FWHM. These IRF values are dominated by timing drift over the course of the experiment, and not by the duration of the individual pulses. The pump fluence of 1.7 mJ/cm² at 400 nm for Ne conditions corresponds to an average excitation fraction of 14% per iridium center, while 1.1 mJ/cm² at 400 nm for Ar conditions corresponds to an average excitation fraction of 9% per iridium center. To avoid sample damage during transient data collection, samples are raster scanned, gas cooled using N_2,[48] and regularly checked for damage by retaking the ground-state XUV spectrum.

Results

Ground-State XUV Spectroscopy. The spectrum of the O_3- and $N_{6,7}$-edge XANES of Ir(III)(ppy)$_3$ is shown in Figure 1A. The O_3-edge appear as a broad feature with a peak at 54.1 eV. The $N_{6,7}$-edges appear at higher energy than the O_3-edge as narrower peaks at 64.4 (N_7) and 67.4 eV (N_6). The 3.0 eV split between N-edges arises from spin-orbit coupling (SOC) induced by the heavy metal center and is consistent with free ion XUV examples and observed $4f_{7/2}/4f_{5/2}$ binding energy in XPS.[4921] This split is consistent regardless of oxidation or ligand field as it derives from the SOC of the core hole.

We note two significant differences between these XUV spectra and those of 3d metal complexes.[8,9,11,13,15,16,50] The shapes of $M_{2,3}$-edge XANES (3p → 3d transitions) spectra in this energy region are dominated by the ligand field of the metal center, as the core-hole spin-orbit coupling is small (< 1 eV). In practice, this SOC results simply in broadening of the peaks, as opposed to the distinct L2- and

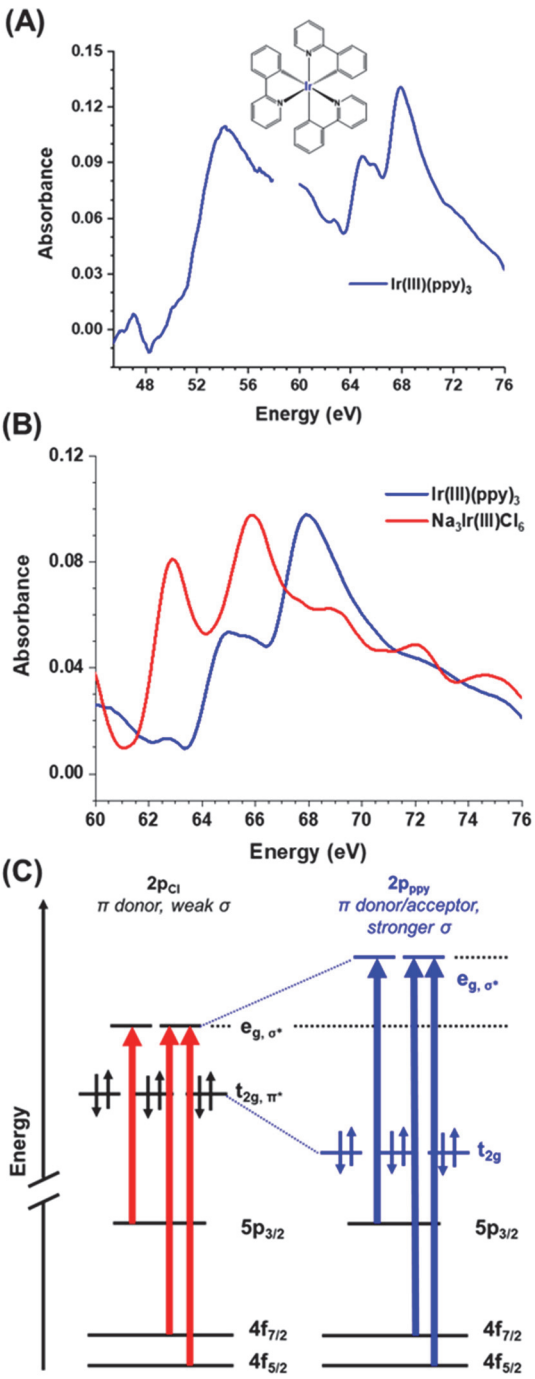

Figure 1 (A) Static O_3- and $N_{6,7}$-edge XANES of Ir(III)(ppy)$_3$, measured using Ar as an HHG medium from 45-58 eV and Ne from 60-66 eV. (B) $N_{6,7}$-edge XANES overlay of Ir(III)(ppy)$_3$ (blue) and $Na_3Ir(III)Cl_6$ (red). (C) Simplified octahedral orbital diagram of changes in the Ir(III) 5d-orbital manifold from chloride to 2-phenylpyridine (ppy) ligands.

L_3 -edges observed for the 2p → 3d transitions in 3d metals. For 5d metals, even the "semi-core" 4f and 5p orbitals have large SOC (~3 and 15 eV, respectively). One obvious manifestation of this SOC is the presence of both $4f_{7/2}$ and $4f_{5/2}$ features in the absorption spectrum. The SOC also impact the selection rules for these features: the O_2 edge ($5p_{1/2}$

$\rightarrow e_g$) is not observed due to $\Delta J = \pm 0,1$ selection rules as discussed in further detail below.

Significant edge shifts occur in the O and N-edges of iridium as a function of the ligand field strength. In comparing $Na_3Ir(III)Cl_6$ with $Ir(III)(ppy)_3$, the $N_{6,7}$- and O_3-edges blueshift by approximately 2 eV when going from $Ir(III)Cl_6^{3-}$ to $Ir(III)(ppy)_3$ ($N_{6,7}$-edges shown in Fig. 1B; O_3-edges in Fig. S2). This is attributed to the stronger ligand field of the latter complex. Cl^- is a weaker sigma donor compared to 2-phenylpyridine's N_{py} and C^-; the ppy ligand will result in higher energies for the empty e_g d-orbitals compared to the chloride ligand and is consistent with the significant blue edge shift for both edges (Fig. 1C). Similar shifts based on ligand field strengths have also been noted at the $L_{2,3}$-edges for 3rd row metals; a recent example with platinum macrocyclic compounds showed that exchanging weaker field ligands (porphyrin, chloride) for stronger field ligands (corrole, pyridine, alkyl) in octahedral Pt(IV) compounds resulted in a 0.4 eV blue shift of the Pt L_3-edge.[51] This shift was caused by the corresponding rise in the d-orbital manifold due to the strengthened ligand interactions. While the shift observed in this work between the iridium(III) species is larger (2 eV vs 0.4 eV), this can be attributed to the more dramatic ligand field strength difference of six chloride ligands versus three bidentate 2-phenylpyridine ligands. This shift shows that O_3- and $N_{6,7}$-edges can be used to track changes in ligand field on the metal center, both as a result of ligand substitution and after photoexcitation (as shown below).

Transient XUV Spectroscopy. Transient O_3-edge and $N_{6,7}$-edge XANES were used to investigate the excited-state dynamics of $Ir(III)(ppy)_3$ upon singlet metal-to-ligand charge transfer (^{1}MLCT) band excitation at 400 nm. $Ir(III)(ppy)_3$ serves as an excellent initial target for transient XUV spectroscopy due to its well-studied photochemistry,[34,35,39,40,42,46,52–62] applicability as a dopant for OLEDs,[33,35,63] and common use as a photosensitizer and catalyst in organic transformations.[24–26,29] Examining the UV-Vis spectrum of $Ir(III)(ppy)_3$ (Fig. 2), three main bands are present: one below than 300 nm that corresponds to singlet π-π* transitions from the 2-phenylpyridine ligand, a broad band centered at 375 nm that corresponds to a ^{1}MLCT (d-π*) transition, and lower intensity triplet MCLT (^{3}MLCT) bands clustered between 430-500 nm.[39,40,46] Prior studies have found that for $Ir(III)(ppy)_3$, the lowest excited state is a triplet metal-to-ligand charge transfer (^{3}MLCT) corresponding to electron transfer from occupied Ir 5d to unoccupied ppy-π* orbitals, with an emission lifetime on the order of microseconds (μs).[40,46,57] Previous optical transient absorption (OTA) and photoluminescence (PL) decay studies have shown that after 400 nm excitation, the ^{1}MLCT state rapidly (≤ 70 fs) undergoes intersystem crossing (ISC) to the ^{3}MLCT state manifold; this triplet state undergoes intramolecular vibrational relaxation (IVR) and vibrational cooling on the order of 200 fs to 5 ps, before slowly relaxing back down to the singlet ground state on the order of nano- to microseconds.[33,39,40,46,47,52,56,57,64] Transient $L_{2,3}$-edge XANES of $Ir(III)(ppy)_3$ with ~100 ps time resolution has been performed in the 11.2-11.3 (L_3) and 12.8-13.0 (L_2) keV region at a synchrotron light source, revealing two key features: a lower energy absorption arising from the core electrons into the photoinduced 5d vacancy for the L_3-edge and a blue-shifted positive absorption corresponding to an oxidation state increase at the iridium center at both L_3- and L_2-edges.[61,65] The authors assigned these features to the ^{3}MLCT state and derived an excited state $10Dq$ of ~6.45 ± 0.20 eV. However, this work primarily focused on this emitting triplet state rather than the early relaxation. Nanosecond transient L_3 XANES of $[Ir(Chp)_2(ddtbbpy)]^+$, picosecond transient L_3 X-ray absorption of $Ir(III)(ppy)_2(bpy)^+$, and femtosecond X-ray transient absorption spectroscopy of $Ir(III)(ppy)_2(ppz)$ at a free-electron laser showed similar spectral features for the triplet MLCT states.[66–68]

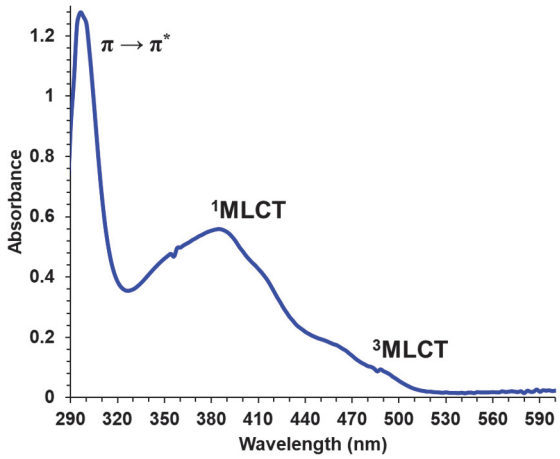

Figure 2 UV-Visible spectrum of a 114-nm thick film of $Ir(III)(ppy)_3$ on glass.

In the current work, transient absorption spectroscopy was performed using Ar as a HHG medium for the O_3-edge and Ne for the $N_{6,7}$- edges. We performed transient O_3-edge XANES of $Ir(III)(ppy)_3$ using 400 nm excitation, with an excitation fraction of ~9%. Time zero and the IRF of 123 fs for these experiments were independently measured by transient XANES of PbI_2 at the iodine $N_{4,5}$-edge. Figure 3A shows averaged spectral slices at select delay times from -250 fs to 100 ps overlaid on the static O_3-edge spectrum of $Ir(III)(ppy)_3$. Upon excitation, a positive feature centered at 48.3 eV appears, along with minor bleach features below 43 eV and weaker higher energy features between 50-57 eV. Within the first few hundred femtoseconds these features have reached their maxima and start to decay (Fig. S5, S7). By 10 ps, all these features have flattened out and are still present at 100 ps, the longest delay time probed.

Transient $N_{6,7}$-edge XANES spectra of $Ir(III)(ppy)_3$ are shown in Figure 3B, overlaid with the ground-state spectrum. Upon excitation, negative features appear at 64.5 and 67.5 eV along with a positive feature at 60.1 eV, with additional weak positive features centered at ~66 eV and 68-70 eV. Within the first few hundred femtoseconds these

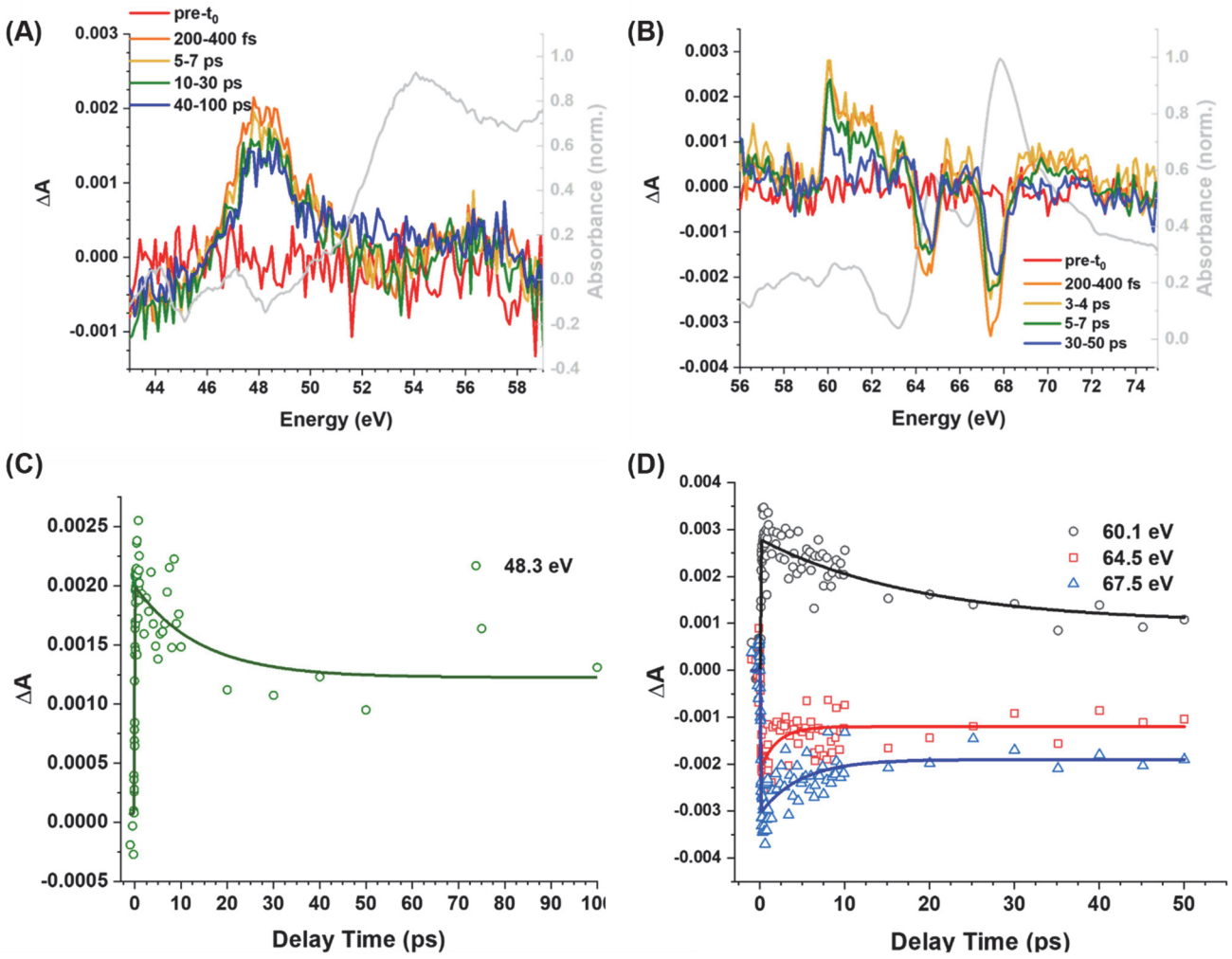

Figure 3 Transient O_3- (A) and $N_{6,7}$-edge (B) XANES spectra of $Ir(III)(ppy)_3$ at select averaged time delays with 400 nm excitation. The static ground state for the respective O_3- and $N_{6,7}$-edges are overlaid as the grey traces. Kinetic traces (circles) of transient O_3- and $N_{6,7}$-edge XANES features with fit as (solid) line. (C) 48.3 eV positive feature from transient O_3–edge spectra; (D) 60.1 eV positive feature (black, circles) and 64.5 (red, squares) & 67.5 eV (blue, triangles) negative features from transient $N_{6,7}$–edge spectra.

features have reached their maxima and start to decrease (Fig. S6, S8). By 10 ps, all these features have flattened and remain so through the later delay times (up to 50 ps).

Single-energy kinetic analysis at three key transient $N_{6,7}$-edge features (60.1 eV absorption, and 64.5 & 67.5 eV bleaches) were undertaken, and the traces are shown in Figure 3C (early delay times shown in Fig. S8). Due to low signal-to-noise for the approximately 66 and 69 eV absorptions, reliable kinetic analysis could not be completed. For the three features tracked, each could be fit as an exponential decay with a shelf that corresponds to the 1.5 μs[40] ^{3}MLCT lifetime. The lifetimes of the exponential decay component are tabulated in Table 1. Single energy kinetic analysis of the positive feature from transient O_3-edge at 48.3 eV was also performed, and the trace is shown in Figure 3D (early delay times shown in Fig. S7). This was fitted to an exponential decay with a long-time shelf shown in Table 1.

Energy (eV)	τ (ps)
48.3	14 ± 6
60.1	19 ± 3
64.5	2.0 ± 0.7
67.5	4.8 ± 0.9

Table 1 Lifetimes at key energies from transient O_3-and $N_{6,7}$-edge XANES spectra.

Discussion

Figure 4A displays the transitions that occur in the ground state compared to the MLCT excited state for $Ir(III)(ppy)_3$ in a simplified orbital diagram. For 3rd row metals, the observed transitions primarily arise due to dipole-allowed transitions of core electrons to empty bound states with selection rules of $\Delta L = 0, \pm 1$ and $\Delta J = 0, \pm 1$, where L and J are the orbital and total angular momentum, respectively. The core-hole with spin S=1/2 couples to the respective core orbital with L character to give $J = |L \pm S|$ states. The 4f core orbital with L=3 will produce the spin-orbit-coupled $4f_{5/2}$ (J=L-S) and $4f_{7/2}$ (J=L+S) states, and the 5p core (L = 1) is split into $5p_{1/2}$ and $5p_{3/2}$. The 5d orbitals (L = 2) will split into either $5d_{5/2}$ or $5d_{3/2}$ states. $Ir(III)(ppy)_3$ is

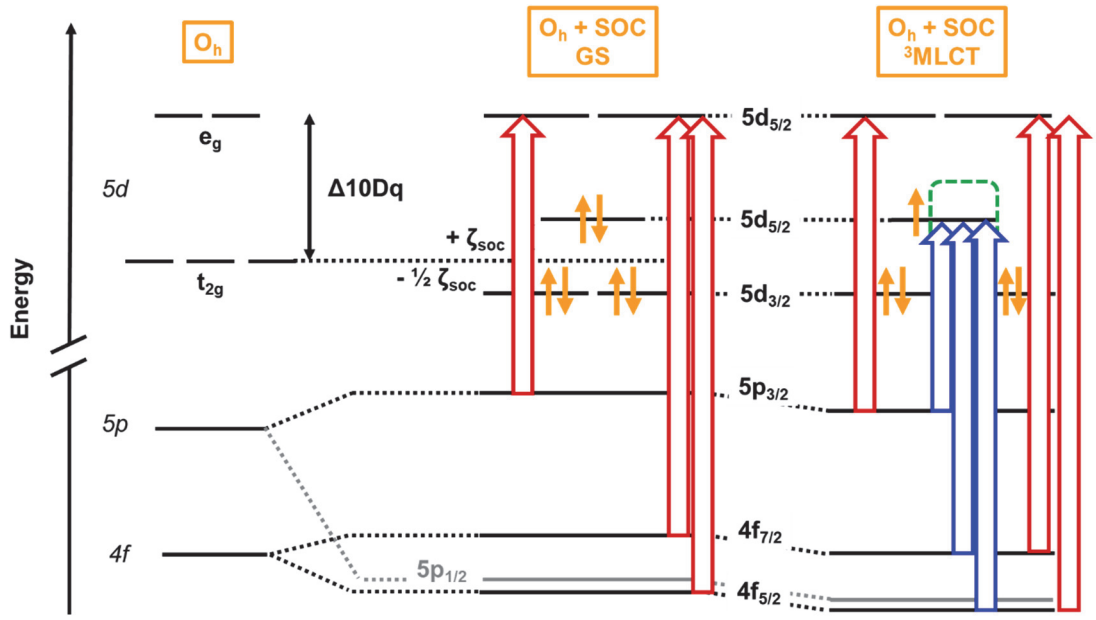

Figure 4 Simplified orbital diagram for allowed XUV transitions from the core 5p and 4f orbitals to valence 5d orbitals in the ground state versus excited MLCT state in Ir(III)(ppy)$_3$.

C_3 symmetric, leading to the 5d orbital manifold depicted in Figure S9, but can generally be simplified to pseudo-octahedral (O_h) due to the large crystal field splitting.[65] Given the presence of both spin-orbit coupling (SOC) and an approximately octahedral ligand field, the 5d orbital manifold will result in predominantly J = 5/2 states for the empty e_g set of orbitals and two sublevels from the t_{2g} set where J = 5/2 for the upper state and J = 3/2 for the doubly-degenerate lower state shown in Figure 4. A more in-depth description of determination of states is described in references [69] (generally for a cubic system) and [45,65,70] (in lower-symmetric systems).

The O_2-edge ($5p_{½} \rightarrow 5d$) is not evident in our experimental data for either Ir(III)(ppy)$_3$ or $Na_3Ir(III)Cl_6$. Transitions from the $5p_{1/2}$ are only allowed when an available 5d orbital has J = 3/2 character, as the other potential transition ($5p_{1/2}$ to $5d_{5/2}$) is forbidden due to Δj = +2. Additionally, due to the Ir 5p SOC of ~15 eV as derived from XPS,[71] any O_2 transitions would at least be partially overlapped with transitions from the $N_{6,7}$-edges. Indeed, a prior photoionization experiment with atomic Ir in the XUV energy range showed very weak $5p_{1/2}$-based transitions nearly overlapped with strong $4f_{7/2,5/2}$-based transitions.[21] It has also been noted that the theoretical cross-section ratio between the $5p_{1/2}$ and 4f peaks yields at most 2% for XPS photon energies, and XPS fitting for Ir 4f binding energies generally ignore $5p_{1/2}$ contributions.[49,71,72] We expect that the Ir O_2-edge is much weaker than the other edges in this region and likely subsumed within the $N_{6,7}$ transitions, and is thus not directly observed here. In an appropriate system that furnishes available $5d_{1/2}$ states, the O_2-edge for a 3rd row transition metal coordination complex can be observed; see the supporting information for a platinum(II) example where a weak O_2-edge is present. However, transitions from the $5p_{3/2}$, $4f_{7/2}$, and $4f_{5/2}$ core orbitals are allowed to either $5d_{5/2}$ or $5d_{3/2}$ empty orbitals, resulting in the observed O_3 , N_7-, and N_6-edges for Ir(III)(ppy)$_3$, respectively, shown in Figure 4.

In the MLCT excited state, a hole is generated in the occupied t_{2g} orbital, resulting in new allowed transitions from the core orbitals to this vacancy. Transient $L_{2,3}$-edge XANES of Ir(III)(ppy)$_3$ indicated that the 5d vacancy is J = 5/2, as a lower energy positive feature appears in transient L_3-edge ($2p_{3/2}$, Δj = +1) that is not present by transient L_2-edge XANES ($2p_{1/2}$, Δj = +2).[65] The same selection rules hold for the $5p \rightarrow t_{2g}$ transitions in this work, with $5p_{1/2} \rightarrow 5d_{t2g}$ forbidden and $5p_{3/2} \rightarrow 5d_{t2g}$ allowed. The latter is observed as the positive transient feature centered at 48.3 eV. Transitions from both $4f_{7/2}$ and $4f_{5/2}$ to the $5d_{5/2}$ t_{2g} vacancy are allowed, resulting in the transient set of doublet-like features at 60.1 and 63.1 eV for transient $N_{6,7}$-edge XANES. Finally, we note that in the MLCT state the core $\rightarrow e_g^1$ transition could create either a singlet or a triplet e_g^2 state, resulting in a splitting of the core $\rightarrow e_g$ absorption peaks. In practice, this splitting is small enough that it is not observed in either this work or in transient L-edge XANES of Ir and Os complexes.[61,66,67,73–77]

The effective oxidation state change from Ir(III) to Ir(IV) lowers the energy of the core orbitals, which will result in a blueshift of the core $\rightarrow e_g$ transitions. For the $N_{6,7}$ edge, this shift manifests as the derivative-shaped features between 63 and 74 eV. The negative features are more intense than the positive features due to the asymmetry of the ground-state peaks, with a sharper rise on the low-energy side. In the case of the O_3-edge, the ground-state 5p $\rightarrow$ 5d feature is broad, and the expected negative feature around 52 eV is likely obscured by the broad $5p_{3/2} \rightarrow 5d_{t2g}$ absorption. A weak blue-shifted absorption between 53-58 eV can be seen in the 2D contour plot in Figure S5.

The XUV spectra selectively probes the Ir d-orbital manifold and is therefore not expected to distinguish between

the initial ^{1}MLCT excited state and the ^{3}MLCT state that forms in tens of femtoseconds. The resulting transient features thus arise from the ^{3}MLCT manifold and relaxation dynamics within or from this manifold. The transient O_3 positive feature is ~5.8-6.0 eV from the ground-state edge, in agreement with the ~5.9 eV energy difference between the analogous features in transient L_3-edge XANES and consistent with an excited state $10D_q$ value of 6.5 eV predicted from density functional theory computations.[53,61,65] There is only a weak bleach feature and blue-shifted positive absorption by transient O_3-edge, likely arising from distribution of the depletion over the broad O_3-edge in the GS convoluted with potential blue shift of the O_3-edge in the oxidized excited state (see Figure S5 for a 2D transient O_3-edge plot at early delay times) at 53.5-54 eV and 54-57 eV, respectively.

A surprising result of the kinetic fitting is the difference in decay times between features corresponding to the t2g hole (the positive features at 48.3 eV and 60.1 eV eV) and those corresponding to the e_g orbitals (the derivative-shaped features from ~63-72 eV). The t_{2g} features decay with a lifetime of ~16 ps before reaching their plateaus, while the e_g features relax in only ~3-4 ps before plateauing. The difference in lifetimes between these two types of features indicates that they report on different relaxation modes. Prior computational work has shown changes in the Ir-C_{ppy}/N_{ppy} bonds in the ^{3}MLCT excited state compared to the ground state Ir(III)$(ppy)_3$,[52,53,59,60,62] indicating a geometric distortion in the triplet state that could be coupled to different vibrational modes.[53,62] Transient optical and luminescence absorption of Ir(III)$(ppy)_3$ in THF also observed a decay with a ~3 ps lifetime which was assigned to vibrational cooling to the surrounding matrix.[40,46,56] This likely corresponds to the 3-4 ps decay components of the e_g features. The derivative-shaped transient results from a blueshift of the 4f → 5d transition in the excited state vs the ground state. We attribute the 30% loss of intensity in these features to vibrational relaxation of the Ir(IV) MLCT state, which redistributes partial charge back onto the Ir, making it more Ir(III)-like. As shown in Figure S9, the transient spectrum immediately after photoexcitation is consistent with a 0.5 eV blueshift of the 4f → e_g transitions in the MLCT state. After the few ps decay, the spectrum matches a 0.3 eV blueshift. This reduction in the blueshift is consistent with density functional theory calculations showing that approximately half of the excess charge on the Ir is lost as the ^{3}MLCT state relaxes from its Franck-Condon geometry (Table S2). We note that similar core-level shifts were observed in transient L-edge XANES of iridium and osmium complexes.[61,66,67,73–77]

A different explanation must be invoked for the ~16 ps loss of intensity of the core → t_{2g} hole features, as these are induced absorption features that are not present in the ground state. Given the breadth of the absorption and the noise in the spectrum, the intensity of these peaks are not expected to be sensitive to the small core-level shifts that led to large changes in the derivative-shape core → e_g peaks. The intensity change must instead be due to either a loss of population in the excited state or a decrease in the oscillator strength of the transition. As there is no evidence from optical transient absorption spectroscopy of a 30% loss of the ^{3}MLCT state at early times, we therefore postulate that this arises from inhomogeneous metal-ligand bond length redistribution noted in calculations of the ^{3}MLCT state geometry,[52,53,59,60,62] reduces the 4f, 5p → t_{2g} overlap and therefore weakens the transition. Alternatively, a change in metal-ligand covalency as the ligand relaxes could lower the metal character of the hole and reduce the strength of the transition.[78] *Ab initio* calculations of the core to valence transitions along the excited state trajectory will be necessary to confirm these hypotheses for the iridium complex. The RASSCF method was used successfully in the picosecond hard X-ray studies of a similar cyclometalated Ir(III) complex to rationalize the excited-state spectra,[67] and can be combined with molecular dynamics calculations of the ^{3}MLCT relaxation.

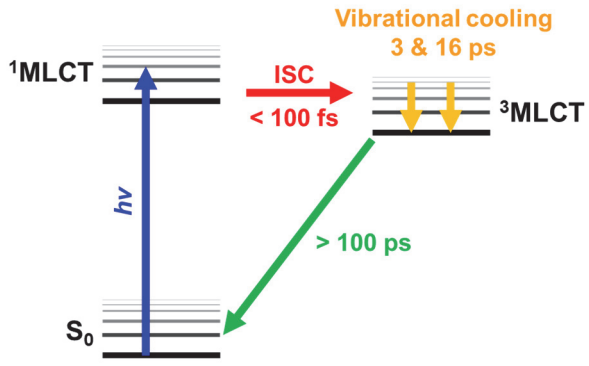

Figure 5. Diagram of Ir$(ppy)_3$ dynamics upon 400 nm excitation derived from transient O_3- and $N_{6,7}$ XANES.

The schematic potential energy surface in Figure 5 summarizes the Ir$(ppy)_3$ dynamics observed in this work. Overall, the combined transient XUV spectroscopy at the O_3- and $N_{6,7}$-edges are in good agreement with known dynamics for 400 nm excitation of the ^{1}MLCT band. Upon 400 nm excitation, there is ultrafast ISC (<90 fs) from the singlet MLCT state to the triplet MLCT state. There is then vibrational relaxation by various modes to the equilibrium ^{3}MLCT state on the order of 200 fs to 15 ps. The final ^{3}MLCT state slowly decays back to the ground state, lasting several orders of magnitude than the delay times collected (up to 100 ps). These results match well to prior ultrafast optical & photoluminescent work examining the manifold, showing that time-resolved XUV be used for tracking metal-based dynamics in iridium complexes.

Finally, we note that the high absorption cross section of the 4f,5p → valence transitions is attractive for pump-probe spectroscopy. A comparison of Figure 1A and Figure 2 reveals that the O_3- and $N_{6,7}$-edge peaks are ~20% as intense as the ^{1}MLCT visible-light transition. The attenuation length of a visible pump and XUV probe are therefore well matched, which simplifies experiment design.

Conclusion

X-ray absorption spectroscopy is a powerful tool for measuring the element-specific electronic structure of complex molecules, and developments in the past two decades have extended its reach to femtosecond timescales

and tabletop sources. We now show that O_3- and $N_{6,7}$-edge XANES spectroscopy can be performed on 3rd-row transition metal complexes with a high-harmonic source, and that the resulting spectra are diagnostic of the ligand field strength and oxidation state of the metal center. Transient absorption spectroscopy of Ir(III)$(ppy)_3$ performed with ~100 fs time resolution shows both the initial formation of an MLCT state and the subsequent vibrational relaxation. This work opens up the possibility of femtosecond O_3- and $N_{6,7}$-edge XANES as a routine spectroscopic technique for the study of molecular complexes relevant to light harvesting and catalysis.

ASSOCIATED CONTENT

Supporting Information. Details of instrumental methods, data processing, and analysis. This material is available free of charge via the Internet at http://pubs.acs.org

AUTHOR INFORMATION

Corresponding Author

* vuraweis@illinois.edu

ACKNOWLEDGMENT

The transient XUV instrument, including the nonlinear optical parametric amplifier, was built with partial funding from the Air Force Office of Scientific Research under AFOSR Awards No. FA9550-14-1-0314 and FA9550-18-1-0293. We thank Dr. Michael Berman and AFOSR for their support of our work, which laid the foundation for this project. This material is based upon work supported by the U.S. Department of Energy, Office of Science, Office of Basic Energy Sciences under Award Number DE-SC0018904. We are grateful to Dr. Frank de Groot for discussion on analysis.

REFERENCES

(1) Kraus, P. M.; Zürch, M.; Cushing, S. K.; Neumark, D. M.; Leone, S. R. The Ultrafast X-Ray Spectroscopic Revolution in Chemical Dynamics. *Nat. Rev. Chem.* **2018**, *2* (6), 82–94. https://doi.org/10.1038/s41570-018-0008-8.

(2) Cirri, A.; Husek, J.; Biswas, S.; Baker, L. R. Achieving Surface Sensitivity in Ultrafast XUV Spectroscopy: M2,3-Edge Reflection-Absorption of Transition Metal Oxides. *J. Phys. Chem. C* **2017**, *121* (29), 15861–15869. https://doi.org/10.1021/acs.jpcc.7b05127.

(3) Geneaux, R.; Marroux, H. J. B.; Guggenmos, A.; Neumark, D. M.; Leone, S. R. Transient Absorption Spectroscopy Using High Harmonic Generation: A Review of Ultrafast X-Ray Dynamics in Molecules and Solids. *Philos. Trans. R. Soc. A Math. Phys. Eng. Sci.* **2019**, *377* (2145). https://doi.org/10.1098/rsta.2017.0463.

(4) Bandaranayake, S.; Hruska, E.; Londo, S.; Biswas, S.; Baker, L. R. Small Polarons and Surface Defects in Metal Oxide Photocatalysts Studied Using XUV Reflection-Absorption Spectroscopy. *J. Phys. Chem. C* **2020**, *124* (42), 22853–22870. https://doi.org/10.1021/acs.jpcc.0c07047.

(5) Schiffmann, A.; Toulson, B. W.; Knez, D.; Messner, R.; Schnedlitz, M.; Lasserus, M.; Hofer, F.; Ernst, W. E.; Gessner, O.; Lackner, F. Ultrashort XUV Pulse Absorption Spectroscopy of Partially Oxidized Cobalt Nanoparticles. *J. Appl. Phys.* **2020**, *127* (18). https://doi.org/10.1063/5.0004582.

(6) Londo, S.; Biswas, S.; Pinchuk, I. V.; Boyadzhiev, A.; Kawakami, R. K.; Baker, L. R. Ultrafast Optical Spin Switching in Ferrimagnetic Nickel Ferrite (NiFe2O4) Studied by XUV Reflection-Absorption Spectroscopy. *J. Phys. Chem. C* **2022**, *126* (5), 2669–2678. https://doi.org/10.1021/acs.jpcc.1c09763.

(7) Klein, I. M.; Liu, H.; Nimlos, D.; Krotz, A.; Cushing, S. K. Ab Initio Prediction of Excited-State and Polaron Effects in Transient XUV Measurements of α-Fe 2 O 3. *J. Am. Chem. Soc.* **2022**, *144* (28), 12834–12841. https://doi.org/10.1021/jacs.2c03994.

(8) Zhang, K.; Ash, R.; Girolami, G. S.; Vura-Weis, J. Tracking the Metal-Centered Triplet in Photoinduced Spin Crossover of Fe(Phen) 3 2+ with Tabletop Femtosecond M-Edge X-Ray Absorption Near-Edge Structure Spectroscopy. *J. Am. Chem. Soc.* **2019**, *141* (43), 17180–17188. https://doi.org/10.1021/jacs.9b07332.

(9) Zhang, K.; Lin, M. F.; Ryland, E. S.; Verkamp, M. A.; Benke, K.; De Groot, F. M. F.; Girolami, G. S.; Vura-Weis, J. Shrinking the Synchrotron: Tabletop Extreme Ultraviolet Absorption of Transition-Metal Complexes. *J. Phys. Chem. Lett.* **2016**, *7* (17), 3383–3387. https://doi.org/10.1021/acs.jpclett.6b01393.

(10) Biswas, S.; Baker, L. R. Extreme Ultraviolet Reflection-Absorption Spectroscopy: Probing Dynamics at Surfaces from a Molecular Perspective. *Acc. Chem. Res.* **2022**, 55 (6), 893–903. https://doi.org/10.1021/acs.accounts.1c00765.

(11) Ryland, E. S.; Zhang, K.; Vura-Weis, J. Sub-100 Fs Intersystem Crossing to a Metal-Centered Triplet in Ni(II)OEP Observed with M-Edge XANES. *J. Phys. Chem. A* **2019**, *123* (25), 5214–5222. https://doi.org/10.1021/acs.jpca.9b03376.

(12) Vura-Weis, J.; Jiang, C. M.; Liu, C.; Gao, H.; Lucas, J. M.; De Groot, F. M. F.; Yang, P.; Alivisatos, A. P.; Leone, S. R. Femtosecond M2,3-Edge Spectroscopy of Transition-Metal Oxides: Photoinduced Oxidation State Change in α-Fe2O3. *J. Phys. Chem. Lett.* **2013**, *4* (21), 3667–

3671. https://doi.org/10.1021/jz401997d.

(13) Ryland, E. S.; Lin, M.-F.; Verkamp, M. A.; Zhang, K.; Benke, K.; Carlson, M.; Vura-Weis, J. Tabletop Femtosecond M-Edge X-Ray Absorption Near-Edge Structure of FeTPPCl: Metalloporphyrin Photophysics from the Perspective of the Metal. *J. Am. Chem. Soc.* **2018**, *140* (13), 4691–4696. https://doi.org/10.1021/jacs.8b01101.

(14) Chatterley, A. S.; Lackner, F.; Pemmaraju, C. D.; Neumark, D. M.; Leone, S. R.; Gessner, O. Dissociation Dynamics and Electronic Structures of Highly Excited Ferrocenium Ions Studied by Femtosecond Xuv Absorption Spectroscopy. *J. Phys. Chem. A* **2016**, *120* (48), 9509–9518. https://doi.org/10.1021/acs.jpca.6b09724.

(15) Ash, R.; Zhang, K.; Vura-Weis, J. Photoinduced Valence Tautomerism of a Cobalt-Dioxolene Complex Revealed with Femtosecond M-Edge XANES. *J. Chem. Phys.* **2019**, *151* (10), 104201. https://doi.org/10.1063/1.5115227.

(16) Shari'ati, Y.; Vura-Weis, J. Ballistic Δ S = 2 Intersystem Crossing in a Cobalt Cubane Following Ligand-Field Excitation Probed by Extreme Ultraviolet Spectroscopy. *Phys. Chem. Chem. Phys.* **2021**, *23* (47), 26990–26996. https://doi.org/10.1039/D1CP04136C.

(17) Haensel, R.; Radler, K.; Sonntag, B.; Kunz, C. Optical Absorption Measurements of Tantalum, Tungsten, Rhenium and Platinum in the Extreme Ultraviolet. *Solid State Commun.* **1969**, *7* (20), 1495–1497. https://doi.org/10.1016/0038-1098(69)90028-3.

(18) Costello, J. T.; Kennedy, E. T.; Sonntagi, B. F.; Cromer, C. L. Xuv Photoabsorption of Laser-Generated w and Pt Vapours. *J. Phys. B At. Mol. Opt. Phys.* **1991**, *24* (24), 5063–5069. https://doi.org/10.1088/0953-4075/24/24/005.

(19) Sladeczek, P.; Martins, M.; Richter, M.; Selbmann, K. H.; Zimmermann, P. Photoionization Experiments on Atomic Pt in the Range 40-90 Ev. *J. Phys. B At. Mol. Opt. Phys.* **1994**, *27* (18), 4123–4131. https://doi.org/10.1088/0953-4075/27/18/012.

(20) Su, M. G.; Dong, C. Z.; Murphy, N.; O'Sullivan, G. Analysis of the Xuv Photoabsorption Spectrum of Au2+, Au3+, and Au4+. *Phys. Rev. A - At. Mol. Opt. Phys.* **2009**, *79* (4), 1–8. https://doi.org/10.1103/PhysRevA.79.042507.

(21) Martins, M.; Sladeczek, P.; Tiedtke, K.; Zimmermann, P. Vacuum Ultraviolet Photoionization Study of Atomic Ir in the Region of the 5p and 4f Excitation. *Phys. Rev. A* **1997**, *55* (1), R8–R9. https://doi.org/10.1103/PhysRevA.55.R8.

(22) Martins, M.; Sladeczek, P.; Tiedtke, K.; Zimmermann, P. Vacuum Ultraviolet Photoionization of the 5d Elements in the Region of the 5p and 4f Excitation. *Eur. Phys. J. D - At. Mol. Opt. Phys.* **1998**, *1* (1), 47–52. https://doi.org/10.1007/s100530050062.

(23) Chang, H. T.; Guggenmos, A.; Chen, C. T.; Oh, J.; Géneaux, R.; Chuang, Y. De; Schwartzberg, A. M.; Aloni, S.; Neumark, D. M.; Leone, S. R. Coupled Valence Carrier and Core-Exciton Dynamics in WS2 Probed by Few-Femtosecond Extreme Ultraviolet Transient Absorption Spectroscopy. *Phys. Rev. B* **2021**, *104* (6), 1–14. https://doi.org/10.1103/PhysRevB.104.064309.

(24) Chan, A. Y.; Perry, I. B.; Bissonnette, N. B.; Buksh, B. F.; Edwards, G. A.; Frye, L. I.; Garry, O. L.; Lavagnino, M. N.; Li, B. X.; Liang, Y.; Mao, E.; Millet, A.; Oakley, J. V.; Reed, N. L.; Sakai, H. A.; Seath, C. P.; MacMillan, D. W. C. Metallaphotoredox: The Merger of Photoredox and Transition Metal Catalysis. *Chem. Rev.* **2022**, *122* (2), 1485–1542. https://doi.org/10.1021/acs.chemrev.1c00383.

(25) Cannalire, R.; Pelliccia, S.; Sancineto, L.; Novellino, E.; Tron, G. C.; Giustiniano, M. Visible Light Photocatalysis in the Late-Stage Functionalization of Pharmaceutically Relevant Compounds. *Chem. Soc. Rev.* **2021**, *50* (2), 866–897. https://doi.org/10.1039/docs00493f.

(26) Monti, F.; Baschieri, A.; Sambri, L.; Armaroli, N. Excited-State Engineering in Heteroleptic Ionic Iridium(III) Complexes. *Acc. Chem. Res.* **2021**, *54* (6), 1492–1505. https://doi.org/10.1021/acs.accounts.0c00825.

(27) Genzink, M. J.; Kidd, J. B.; Swords, W. B.; Yoon, T. P. Chiral Photocatalyst Structures in Asymmetric Photochemical Synthesis. *Chem. Rev.* **2022**, *122* (2), 1654–1716. https://doi.org/10.1021/acs.chemrev.1c00467.

(28) Schmid, L.; Glaser, F.; Schaer, R.; Wenger, O. S. High Triplet Energy Iridium(III) Isocyanoborato Complex for Photochemical Upconversion, Photoredox and Energy Transfer Catalysis. *J. Am. Chem. Soc.* **2022**, *144* (2), 963–976. https://doi.org/10.1021/jacs.1c11667.

(29) Diluzio, S.; Connell, T. U.; Mdluli, V.; Kowalewski, J. F.; Bernhard, S. Understanding Ir(III) Photocatalyst Structure-Activity Relationships: A Highly Parallelized Study of Light-Driven Metal Reduction Processes. *J. Am. Chem. Soc.* **2022**, *144* (3), 1431–1444. https://doi.org/10.1021/jacs.1c12059.

(30) Nacsa, E. D.; MacMillan, D. W. C. Spin-Center Shift-Enabled Direct Enantioselective α-Benzylation of Aldehydes with Alcohols. *J. Am. Chem. Soc.* **2018**, *140* (9), 3322–3330. https://doi.org/10.1021/jacs.7b12768.

(31) Joe, C. L.; Doyle, A. G. Direct Acylation of C(Sp3)-H Bonds Enabled by Nickel and Photoredox Catalysis. *Angew. Chemie - Int. Ed.* **2016**, *55* (12), 4040–4043. https://doi.org/10.1002/anie.201511438.

(32) Holmberg-Douglas, N.; Nicewicz, D. A. Photoredox-Catalyzed C–H Functionalization Reactions. *Chem. Rev.* **2022**, *122* (2), 1925–2016. https://doi.org/10.1021/acs.chemrev.1c00311.

(33) Gildea, L. F.; Williams, J. A. G. *Iridium and Platinum Complexes for OLEDs*; Woodhead Publishing Limited, 2013. https://doi.org/10.1533/9780857098948.1.77.

(34) Deaton, J. C.; Castellano, F. N. Archetypal Iridium(III) Compounds for Optoelectronic and Photonic Applications. In *Iridium(III) in Optoelectronic and Photonics Applications*; John Wiley & Sons, Ltd: Chichester, UK, 2017; pp 1–69. https://doi.org/10.1002/9781119007166.ch1.

(35) Adachi, C.; Baldo, M. A.; Forrest, S. R.; Thompson, M. E. High-Efficiency Organic Electrophosphorescent Devices with Tris(2-Phenylpyridine)Iridium Doped into Electron-Transporting Materials. *Appl. Phys. Lett.* **2000**, *77* (6), 904–906. https://doi.org/10.1063/1.1306639.

(36) Wang, Y.; Bao, P.; Wang, J.; Jia, R.; Bai, F. Q.; Zhang, H. X. Comprehensive Investigation into Luminescent Properties of Ir(III) Complexes: An Integrated Computational Study of Radiative and Nonradiative Decay Processes. *Inorg. Chem.* **2018**, *57* (11), 6561–6570. https://doi.org/10.1021/acs.inorgchem.8b00705.

(37) Bevernaegie, R.; Wehlin, S. A. M.; Elias, B.; Troian-Gautier, L. A Roadmap Towards Visible Light Mediated Electron Transfer Chemistry with Iridium(III) Complexes. *ChemPhotoChem* **2021**, *5* (3), 217–234. https://doi.org/10.1002/cptc.202000255.

(38) Huang, H.; Banerjee, S.; Sadler, P. J. Recent Advances in the Design of Targeted Iridium(III) Photosensitizers for Photodynamic Therapy. *ChemBioChem* **2018**, *19* (15), 1574–1589. https://doi.org/10.1002/cbic.201800182.

(39) Ichimura, K.; Kobayashi, T.; King, K. A.; Watts, R. J. Excited-State Absorption Spectroscopy of Ortho-Metalated Iridium(III) Complexes. *J. Phys. Chem.* **1987**, *91* (24), 6104–6106. https://doi.org/10.1021/j100308a012.

(40) Holzer, W.; Penzkofer, A.; Tsuboi, T. Absorption and Emission Spectroscopic Characterization of Ir(Ppy) 3. *Chem. Phys.* **2005**, *308* (1–2), 93–102. https://doi.org/10.1016/j.chemphys.2004.07.051.

(41) Lowry, M. S.; Bernhard, S. Synthetically Tailored Excited States: Phosphorescent, Cyclometalated Iridium(III) Complexes and Their Applications. *Chem. - A Eur. J.* **2006**, *12* (31), 7970–7977. https://doi.org/10.1002/chem.200600618.

(42) Edkins, R. M.; Wriglesworth, A.; Fucke, K.; Bettington, S. L.; Beeby, A.; Flamigni, L.; Barbieri, A.; Sabatini, C.; Ventura, B.; Barigelletti, F.; Singh, A.; Teegardin, K.; Kelly, M.; Prasad, K. S.; Krishnan, S.; Weaver, J. D.; Xu, X.; Yang, X.; Wu, Y.; Zhou, G.; Wu, C.; Wong, W. Y.; You, Y.; Cho, S.; Nam, W. Photochemistry and Photophysics of Coordination Compounds: Iridium\rPhotochemistry and Photophysics of Coordination Compounds II. *Chem. - An Asian J.* **2015**, *10* (June), 252–262.

(43) Bevernaegie, R.; Wehlin, S. A. M.; Piechota, E. J.; Abraham, M.; Philouze, C.; Meyer, G. J.; Elias, B.; Troian-Gautier, L. Improved Visible Light Absorption of Potent Iridium(III) Photo-Oxidants for Excited-State Electron Transfer Chemistry. *J. Am. Chem. Soc.* **2020**, *142* (6), 2732–2737. https://doi.org/10.1021/jacs.9b12108.

(44) Kim, D.; Teets, T. S. Strategies for Accessing Photosensitizers with Extreme Redox Potentials. *Chem. Phys. Rev.* **2022**, *3* (2), 021302. https://doi.org/10.1063/5.0084554.

(45) Yersin, H.; Rausch, A. F.; Czerwieniec, R.; Hofbeck, T.; Fischer, T. The Triplet State of Organo-Transition Metal Compounds. Triplet Harvesting and Singlet Harvesting for Efficient OLEDs. *Coord. Chem. Rev.* **2011**, *255* (21–22), 2622–2652. https://doi.org/10.1016/j.ccr.2011.01.042.

(46) Hofbeck, T.; Yersin, H. The Triplet State of Fac-Ir(Ppy)3. *Inorg. Chem.* **2010**, *49* (20), 9290–9299. https://doi.org/10.1021/ic100872w.

(47) Chergui, M. Ultrafast Photophysics of Transition Metal Complexes. *Acc. Chem. Res.* **2015**, *48* (3), 801–808. https://doi.org/10.1021/ar500358q.

(48) Lin, M.; Verkamp, M. A.; Leveillee, J.; Ryland, E. S.; Benke, K.; Zhang, K.; Weninger, C.; Shen, X.; Li, R.; Fritz, D.; Bergmann, U.; Wang, X.; Schleife, A.; Vura-Weis, J. Carrier-Specific Femtosecond XUV Transient Absorption of PbI 2 Reveals Ultrafast Nonradiative Recombination. *J. Phys. Chem. C* **2017**, *121* (50), 27886–27893. https://doi.org/10.1021/acs.jpcc.7b11147.

(49) Pfeifer, V.; Jones, T. E.; Velasco Vélez, J. J.;

Massué, C.; Arrigo, R.; Teschner, D.; Girgsdies, F.; Scherzer, M.; Greiner, M. T.; Allan, J.; Hashagen, M.; Weinberg, G.; Piccinin, S.; Hävecker, M.; Knop-Gericke, A.; Schlögl, R. The Electronic Structure of Iridium and Its Oxides. *Surf. Interface Anal.* **2016**, *48* (5), 261–273. https://doi.org/10.1002/sia.5895.

(50) Sye, K. M.; Leahy, C. A.; Vura-Weis, J. Low Quantum Efficiency of μ-Oxo Iron Bisporphyrin Photocatalysts Explained with Femtosecond M-Edge XANES. *Catal. Sci. Technol.* **2022**, *1*. https://doi.org/10.1039/d2cy01081j.

(51) Matson, B. D.; Thomas, K. E.; Alemayehu, A. B.; Ghosh, A.; Sarangi, R. X-Ray Absorption Spectroscopy of Exemplary Platinum Porphyrin and Corrole Derivatives: Metal-: Versus Ligand-Centered Oxidation. *RSC Adv.* **2021**, *11* (51), 32269–32274. https://doi.org/10.1039/d1ra06151h.

(52) Kleinschmidt, M.; Van Wüllen, C.; Marian, C. M. Intersystem-Crossing and Phosphorescence Rates in Fac-IrIII(Ppy)3: A Theoretical Study Involving Multi-Reference Configuration Interaction Wavefunctions. *J. Chem. Phys.* **2015**, *142* (9). https://doi.org/10.1063/1.4913513.

(53) Fine, J.; Diri, K.; Krylov, A. I.; Nemirow, C.; Lu, Z.; Wittig, C. Electronic Structure of Tris(2-Phenylpyridine)Iridium: Electronically Excited and Ionized States. *Mol. Phys.* **2012**, *110* (15–16), 1849–1862. https://doi.org/10.1080/00268976.2012.685899.

(54) Nemirow, C.; Fine, J.; Lu, Z.; Diri, K.; Krylov, A. I.; Wittig, C. Photoionization of Tris(2-Phenylpyridine)Iridium. *Mol. Phys.* **2012**, *110* (15–16), 1893–1908. https://doi.org/10.1080/00268976.2012.689871.

(55) Smith, A. R. G.; Burn, P. L.; Powell, B. J. Spin-Orbit Coupling in Phosphorescent Iridium(III) Complexes. *ChemPhysChem* **2011**, *12* (13), 2429–2438. https://doi.org/10.1002/cphc.201100397.

(56) Hedley, G. J.; Ruseckas, A.; Samuel, I. D. W. Ultrafast Luminescence in Ir(Ppy)3. *Chem. Phys. Lett.* **2008**, *450* (4–6), 292–296. https://doi.org/10.1016/j.cplett.2007.11.028.

(57) Finkenzeller, W. J.; Yersin, H. Emission of Ir(Ppy)3. Temperature Dependence, Decay Dynamics, and Magnetic Field Properties. *Chem. Phys. Lett.* **2003**, *377* (3–4), 299–305. https://doi.org/10.1016/S0009-2614(03)01142-4.

(58) Demas, J. N.; Harris, E. W.; Flynn, C. M.; Diemente, D. Luminescent Osmium(II) and Iridium(III) Complexes as Photosensitizers. *J. Am. Chem. Soc.* **1975**, *97* (13), 3838–3839. https://doi.org/10.1021/ja00846a058.

(59) Babazadeh, M.; Burn, P. L.; Huang, D. M. Calculating Transition Dipole Moments of Phosphorescent Emitters for Efficient Organic Light-Emitting Diodes. *Phys. Chem. Chem. Phys.* **2019**, *21* (19), 9740–9746. https://doi.org/10.1039/c9cp01045a.

(60) Smith, A. R. G.; Burn, P. L.; Powell, B. J. Exact Exchange and the Density Functional Theory of Metal-to-Ligand Charge-Transfer in Fac-Ir(Ppy)3. *Org. Electron.* **2016**, *33*, 110–115. https://doi.org/10.1016/j.orgel.2016.02.039.

(61) Göries, D.; Dicke, B.; Roedig, P.; Stübe, N.; Meyer, J.; Galler, A.; Gawelda, W.; Britz, A.; Geßler, P.; Sotoudi Namin, H.; Beckmann, A.; Schlie, M.; Warmer, M.; Naumova, M.; Bressler, C.; Rübhausen, M.; Weckert, E.; Meents, A. Time-Resolved Pump and Probe x-Ray Absorption Fine Structure Spectroscopy at Beamline P11 at PETRA III. *Rev. Sci. Instrum.* **2016**, *87* (5). https://doi.org/10.1063/1.4948596.

(62) Gonzalez-Vazquez, J. P.; Burn, P. L.; Powell, B. J. Interplay of Zero-Field Splitting and Excited State Geometry Relaxation in Fac-Ir(Ppy)3. *Inorg. Chem.* **2015**, *54* (21), 10457–10461. https://doi.org/10.1021/acs.inorgchem.5b01918.

(63) Xu, H.; Chen, R.; Sun, Q.; Lai, W.; Su, Q.; Huang, W.; Liu, X. Recent Progress in Metal-Organic Complexes for Optoelectronic Applications. *Chem. Soc. Rev.* **2014**, *43* (10), 3259–3302. https://doi.org/10.1039/c3cs60449g.

(64) Tang, K. C.; Liu, K. L.; Chen, I. C. Rapid Intersystem Crossing in Highly Phosphorescent Iridium Complexes. *Chem. Phys. Lett.* **2004**, *386* (4–6), 437–441. https://doi.org/10.1016/j.cplett.2004.01.098.

(65) Göries, D. Photoinduced Charge Transfer in a Transition Metal Complex Investigated by Time-Resolved X-Ray Absorption Fine Structure Spectroscopy: Setup and Experiment., Universit¨at Hamburg, 2014.

(66) Choi, J.; Ahn, M.; Lee, J. H.; Ahn, D. S.; Ki, H.; Oh, I.; Ahn, C. W.; Choi, E. H.; Lee, Y.; Lee, S.; Kim, J.; Cho, D. W.; Wee, K. R.; Ihee, H. Ultrafast Excited State Relaxation Dynamics in a Heteroleptic Ir(Iii) Complex,: Fac - Ir(Ppy)2(Ppz), Revealed by Femtosecond X-Ray Transient Absorption Spectroscopy. *Inorg. Chem. Front.* **2021**, *8* (12), 2987–2998. https://doi.org/10.1039/doqi01510e.

(67) Britz, A.; Bokarev, S. I.; Assefa, T. A.; Bajnóczi, È. G.; Németh, Z.; Vankó, G.; Rockstroh, N.; Junge, H.; Beller, M.; Doumy, G.; March, A. M.; Southworth, S. H.; Lochbrunner, S.; Kühn, O.; Bressler, C.; Gawelda, W. Site-Selective Real-Time Observation of Bimolecular Electron

Transfer in a Photocatalytic System Using L-Edge X-Ray Absorption Spectroscopy**. *ChemPhysChem* **2021**, *22* (7), 693–700. https://doi.org/10.1002/cphc.202000845.

(68) Smolentsev, G.; Van Vliet, K. M.; Azzaroli, N.; Van Bokhoven, J. A.; Brouwer, A. M.; De Bruin, B.; Nachtegaal, M.; Tromp, M. Pump-Probe XAS Investigation of the Triplet State of an Ir Photosensitizer with Chromenopyridinone Ligands. *Photochem. Photobiol. Sci.* **2018**, *17* (7), 896–902. https://doi.org/10.1039/c8pp00065d.

(69) Martins, C.; Aichhorn, M.; Biermann, S. Coulomb Correlations in 4d and 5d Oxides from First Principles - Or How Spin-Orbit Materials Choose Their Effective Orbital Degeneracies. *J. Phys. Condens. Matter* **2017**, *29* (26). https://doi.org/10.1088/1361-648X/aa648f.

(70) Nozaki, K. Theoretical Studies on Photophysical Properties and Mechanism of Phosphorescence in [Fac-Ir(2-Phenylpyridine)3]. *J. Chinese Chem. Soc.* **2006**, *53* (1), 101–112. https://doi.org/10.1002/jccs.200600013.

(71) Freakley, S. J.; Ruiz-Esquius, J.; Morgan, D. J. The X-Ray Photoelectron Spectra of Ir, IrO2 and IrCl3 Revisited. *Surf. Interface Anal.* **2017**, *49* (8), 794–799. https://doi.org/10.1002/sia.6225.

(72) Yeh, J. J.; Lindau, I. Atomic Subshell Photoionization Cross Sections and Asymmetry Parameters: $1 \leqslant Z \leqslant 103$. *At. Data Nucl. Data Tables* **1985**, *32* (1), 1–155. https://doi.org/10.1016/0092-640X(85)90016-6.

(73) Mara, M. W.; Phelan, B. T.; Xie, Z. L.; Kim, T. W.; Hsu, D. J.; Liu, X.; Valentine, A. J. S.; Kim, P.; Li, X.; Adachi, S. I.; Katayama, T.; Mulfort, K. L.; Chen, L. X. Unveiling Ultrafast Dynamics in Bridged Bimetallic Complexes Using Optical and X-Ray Transient Absorption Spectroscopies. *Chem. Sci.* **2022**, *13* (6), 1715–1724. https://doi.org/10.1039/d1sc05034f.

(74) Zhao, J.; De Kreijger, S.; Troian-Gautier, L.; Yu, J.; Hu, W.; Zhang, X.; Elias, B.; Moonshiram, D. Deciphering the Photophysical Kinetics, Electronic Configurations and Structural Conformations of Iridium-Cobalt Hydrogen Evolution Photocatalysts. *Chem. Commun.* **2022**, *58* (58), 8057–8060. https://doi.org/10.1039/d2cc02286a.

(75) Smolentsev, G.; Van Vliet, K. M.; Azzaroli, N.; Van Bokhoven, J. A.; Brouwer, A. M.; De Bruin, B.; Nachtegaal, M.; Tromp, M. Pump-Probe XAS Investigation of the Triplet State of an Ir Photosensitizer with Chromenopyridinone Ligands. *Photochem. Photobiol. Sci.* **2018**, *17* (7), 896–902. https://doi.org/10.1039/c8pp00065d.

(76) Zhang, X.; Pápai, M.; Møller, K. B.; Zhang, J.; Canton, S. E. Characterizing the Solvated Structure of Photoexcited [Os(Terpy)2]2+ with X-Ray Transient Absorption Spectroscopy and DFT Calculations. *Molecules* **2016**, *21* (2), 1–9. https://doi.org/10.3390/molecules21020235.

(77) Zhang, X.; Canton, S. E.; Smolentsev, G.; Wallentin, C. J.; Liu, Y.; Kong, Q.; Attenkofer, K.; Stickrath, A. B.; Mara, M. W.; Chen, L. X.; Wärnmark, K.; Sundström, V. Highly Accurate Excited-State Structure of [Os(Bpy)2dcbpy] 2+ Determined by X-Ray Transient Absorption Spectroscopy. *J. Am. Chem. Soc.* **2014**, *136* (24), 8804–8809. https://doi.org/10.1021/ja5040733.

(78) Solomon, E. I.; Hedman, B.; Hodgson, K. O.; Dey, A.; Szilagyi, R. K. Ligand K-Edge X-Ray Absorption Spectroscopy: Covalency of Ligand-Metal Bonds. *Coord. Chem. Rev.* **2005**, *249* (1–2), 97–129. https://doi.org/10.1016/j.ccr.2004.03.020.

Femtosecond extreme ultraviolet spectroscopy of an iridium photocatalyst reveals oxidation state and ligand field specific dynamics.

Clare A. Leahy & Josh Vura-Weis*

University of Illinois at Urbana-Champaign, 606 S. Matthews Ave., Urbana IL, 61801

Table of Contents

Static XUV

All ground state spectra shown in this work are presented after subtraction of a power-law baseline that accounts for photoionization of the valence electrons. The raw absorption spectrum is shown in Figure S1.

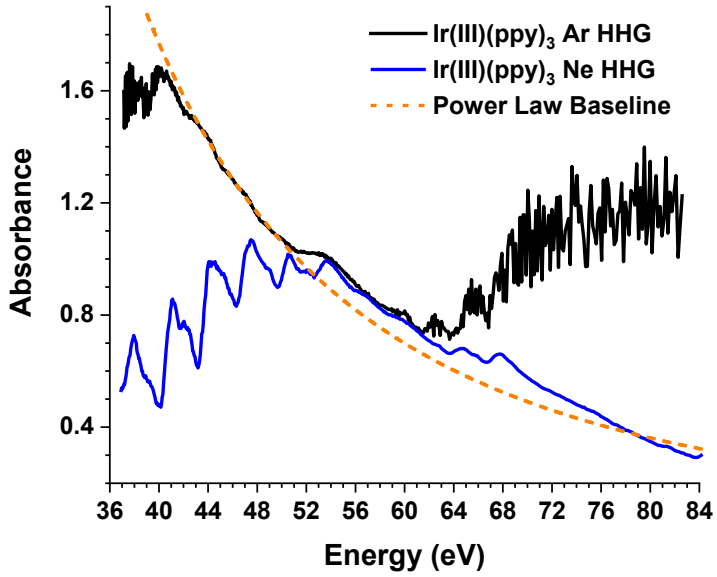

Figure S1. Raw absorption spectra of $Ir(ppy)_3$ using argon HHG conditions for O_3-edge XANES (black line) and neon HHG conditions for $N_{6,7}$-edge XANES (blue line) with the powerbase line (dotted orange line).

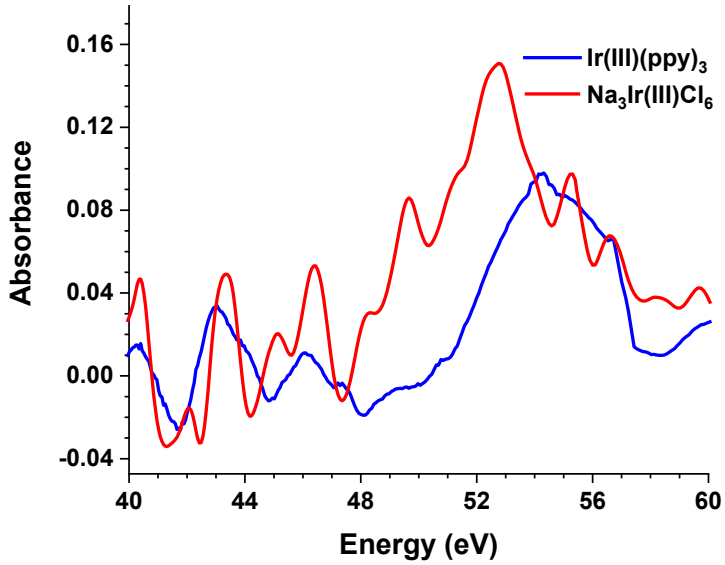

Figure S2. O_3-edge XANES overlay of $Ir(III)(ppy)_3$ (blue) and $Na_3Ir(III)Cl_6$ (red).

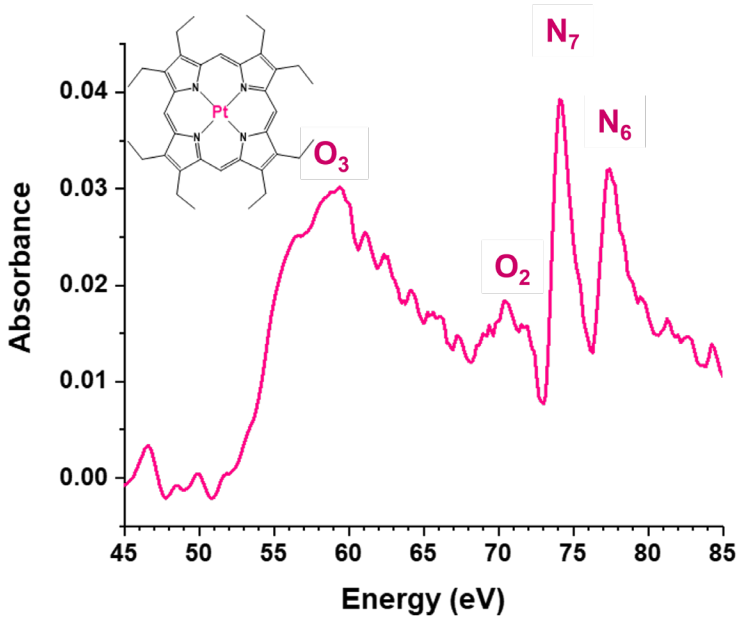

Figure S3. $O_{2,3}$- & $N_{6,7}$-edge XANES of Pt(II)OEP.

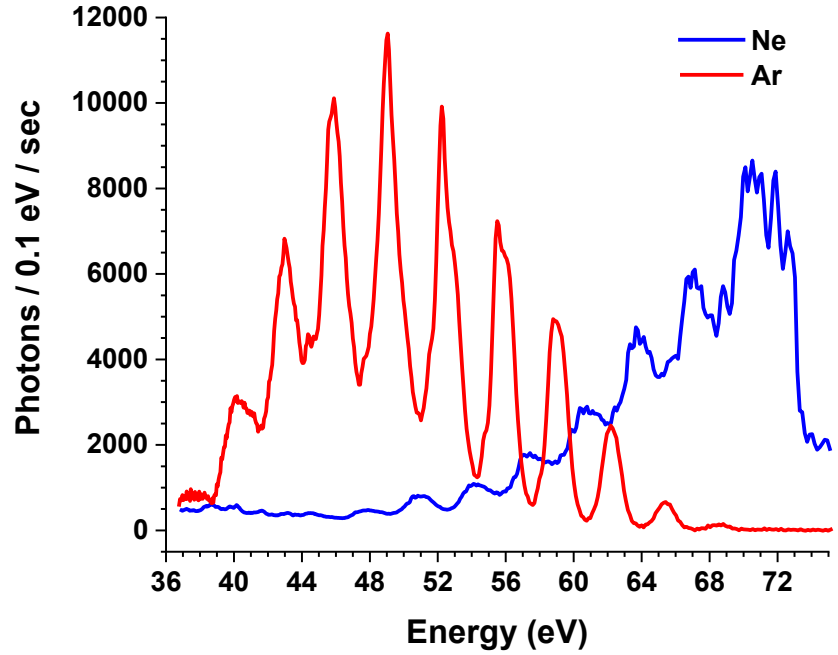

Figure S4. Overlay of HHG XUV harmonic flux (photons/0.1 eV/sec) using Ar (red) and Ne (blue) gas medium through the same thin film Ir(III)$(ppy)_3$ for the static XANES, showing the ~58-59.9 eV energy range provide low continuum flux for ground state experiments.

Transient XUV – 2D Plots

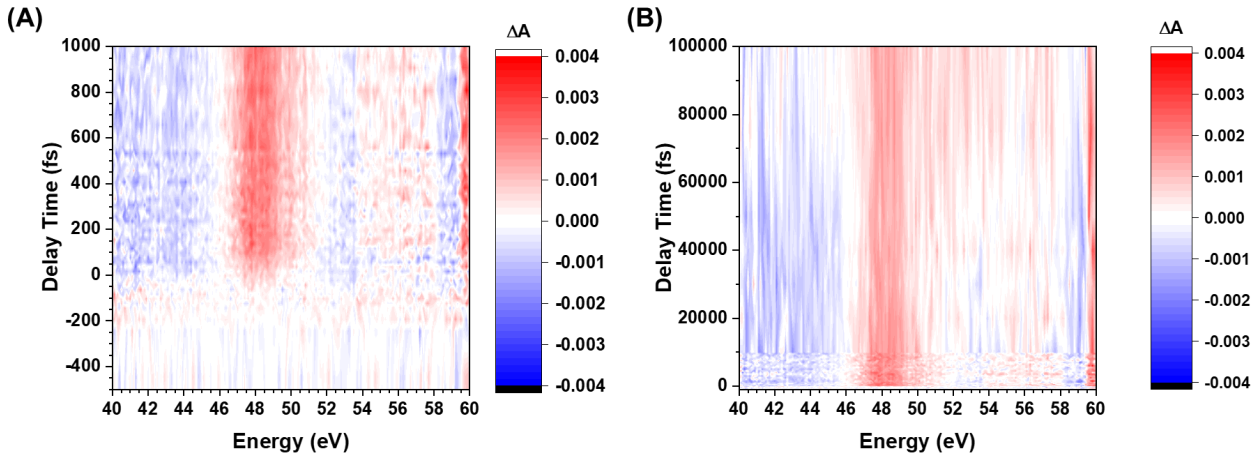

Figure S5. 2D transient O_3-edge XANES of Ir(III)(ppy)$_3$ with 400 nm excitation at early (A) and late (B) delay times.

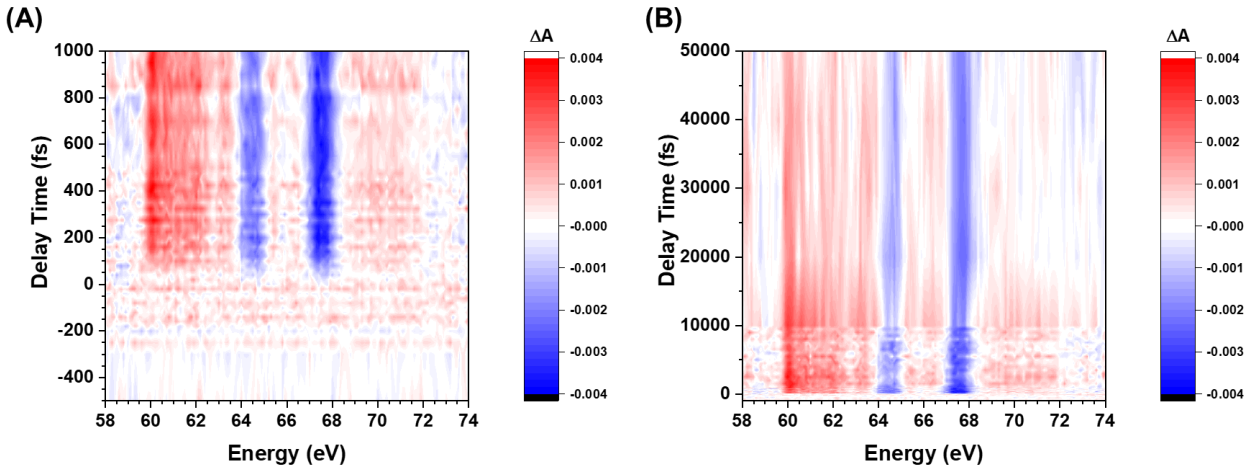

Figure S6. 2D transient $N_{6,7}$-edge XANES of Ir(III)(ppy)$_3$ with 400 nm excitation at early (A) and late (B) delay times.

Transient XUV – Kinetics

Both mono- and bi-exponential sequential decays with a long-time shelf were attempted when performing kinetic analysis at the positive transient O_3 feature at 48.3 eV. A sequential bi-exponential decay using the experimental IRF of 123 fs was attempted to fit the 48.3 eV kinetic data (tabulated in Table S1), but the earlier short time component has a lifetime on the order of the experimental IRF and a standard error nearly as large as the lifetime itself. This suggested while there is potentially an early, short-lived feature on a similar timescale as the ~120 fs IRF, this is convoluted with the IRF rise. This led us to primarily analyze the kinetic data using the mono-exponential decay function as described

in the main text. The kinetic of the transient O_3-edge positive feature match well to the transient $N_{6,7}$-edge positive feature, with the O_3-edge ~16 ps decay component within error of the $N_{6,7}$-edge decay component. No satisfactory bi-exponential kinetic model was found for the transient $N_{6,7}$-edge features, nor was there a delayed rise in these features.

The potential presence of an early, short-lived feature by transient O_3-edge XANES that is not present in transient $N_{6,7}$-edge XANES points to different information gained about the dynamics at each edge. Given that the main difference between the O_3- and $N_{6,7}$-edges are the starting core orbitals, it is likely that the potential short-lived state involves changes in iridium 5p orbital interactions in this state. A recent report by Chang *et. al.* noted that the tungsten O_3- and $N_{6,7}$-edges showed different behavior of core-exciton transitions at the $N_{6,7}$-edge compared to core-to-band transitions at the O_3-edge when tracking the dynamics of photoexcited carriers in WS_2; they postulate that these differences occur based on the difference in degree of localization of the core orbitals.[1]

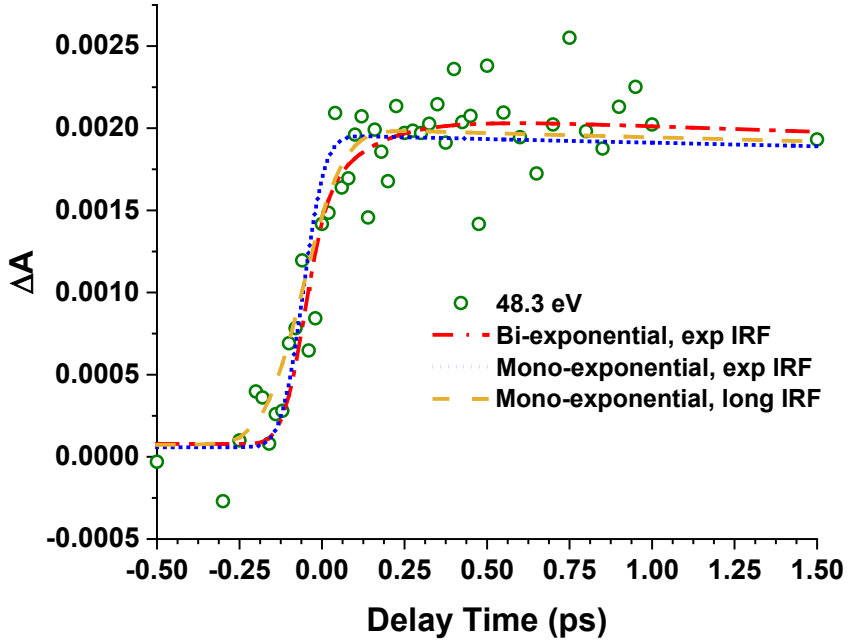

Figure S7. Transient O_3-edge XANES of Ir(III)(ppy)$_3$ with 400 nm excitation show to 1.5 ps delay time – kinetic analysis at 48.3 eV at early times with three different sequential exponential models attempted: bi-exponential with the experimental 123 fs IRF, mono-exponential with the experimental IRF, and mono-exponential allowing the IRF to drift, all with a long-time shelf.

Table S1. Summary of transient O_3-edge kinetic analysis at 48.3 eV using three different sequential exponential decay models with a long-time shelf.

Fit	IRF (fs)	τ_1 (ps)	τ_2 (ps)	Shelf (mA)
Mono-exponential	123	-	16 ± 8	+ 1.2
Mono-exponential	245	-	14 ± 6	+ 1.2
Bi-exponential	123	0.16 ± 0.11	11 ± 3	+ 1.2

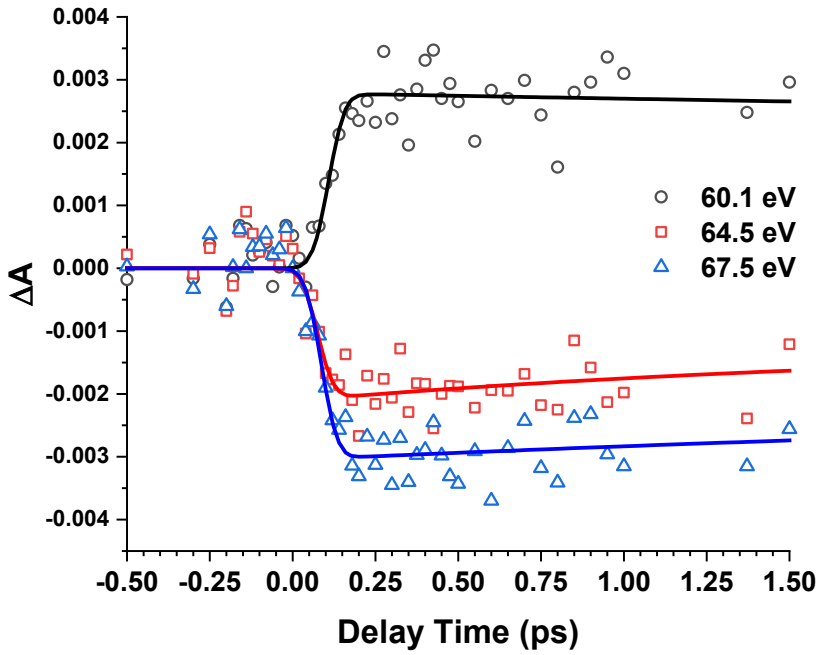

Figure S8. Transient $N_{6,7}$ -edge XANES of Ir(III)(ppy)$_3$ with 400 nm excitation at early delay times (to 1.5 ps) – kinetic analysis at 60.1 (black, circles), 64.4 (red, squares), and 67.4 eV (blue, triangles).

Analysis of core-level shift in MLCT state

An oxidation state increase generally results in a shift of spectral features to higher energies. We therefore modeled the transient spectra in the 4f→eg region of the spectrum as a simple blueshift of the ground-state spectrum, taking into account the 14% excitation fraction. As shown in Figure S9A, the experimental transient spectrum at <1 ps is consistent with a blueshift of 0.5 eV, in regards to both the magnitude of the signal and the asymmetric derivative-like shape. After the initial few-ps decay, the experimental transient spectrum is consistent with a blueshift of 0.3 eV (Figure S9B).

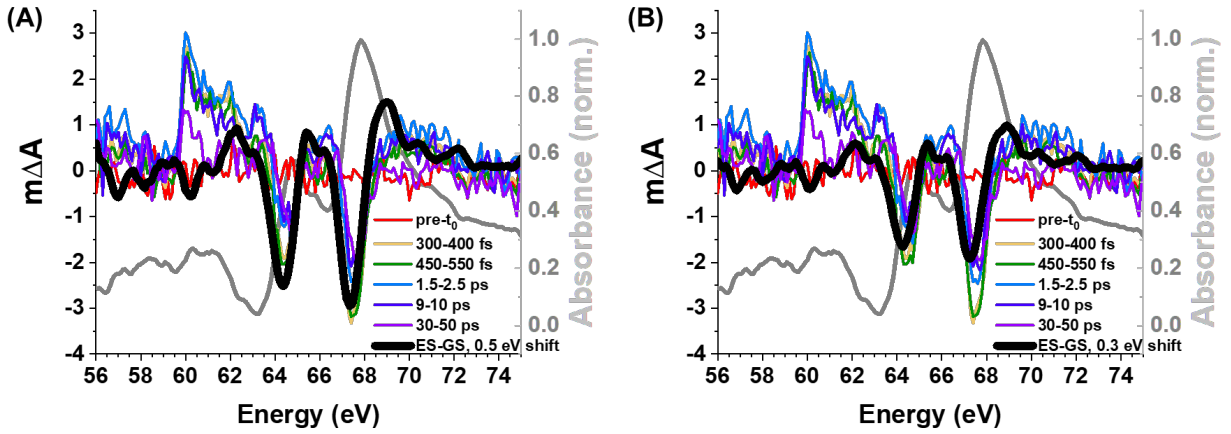

Figure S9. Comparison of the transient $N_{6,7}$-edge XANES spectral slices of $Ir(ppy)_3$ to the difference spectrum (thick black line) of the static $N_{6,7}$-edge subtracted from a predicted excited state spectrum, which is the static spectrum shifted 0.5 eV (A) or 0.3 eV (B) to higher energy as anticipated for an increase in oxidation state at the iridium center.

To estimate the change in the electron density on the Ir after photoexcitation, we performed density functional theory calculations of the Mulliken charge at the metal center in the optimized singlet ground-state geometry, the ^{3}MLCT state at that geometry (i.e. the Franck-Condon state assuming rapid intersystem crossing), and the optimized ^{3}MLCT geometry. We performed these calculations at three levels of theory to ensure that the results were not strongly affected by the basis set and/or environment: first using the B3LYP functional and LANL2DZ pseudopotential/basis set in the gas phase, then using the PCM method to simulate solvation in toluene, then using the def2-TZVP basis set at the B3LYP/LANL2DZ gas-phase optimized geometry. All calculations were performed using Gaussian16.

As shown in Table S2, the amount of excess positive charge on the metal in the nominal Ir(IV) state vs the Ir(III) state decreases by approximately half upon relaxation to the ^{3}MLCT optimal geometry. For example, for the B3LYP/def2-TZVP calculation, the Ir charge is 0.67 in the singlet Ir(III) ground state, 0.82 in the Franck-Condon ^{3}MLCT Ir(IV) state, and 0.75 in the relaxed ^{3}MLCT Ir(IV) state. This approximate halving of the excess charge on the Ir center is consistent with our observation that the 4f→5d blueshift in the ^{3}MLCT state decreases over the first few ps as the ligands reorganize.

Table S2. Charge density on the iridium center in $Ir(ppy)_3$ in the ground and excited state geometries from computational calculations.

Method	Ground state singlet	^{3}MLCT in GS geometry, Δ from GS	^{3}MLCT in optimized geometry, Δ from GS
B3LYP/LANL2DZ	0.74	1.16, +0.42	0.86, +0.12
B3LYP/LANL2DZ in toluene dielectric	0.73	0.92, +0.19	0.84, +0.11
B3LYP/def2-TZVP @ B3LYP/LANL2DZ geometries	0.67	0.82, +0.15	0.75, +0.08

Orbital Manifolds – O_h vs C_3

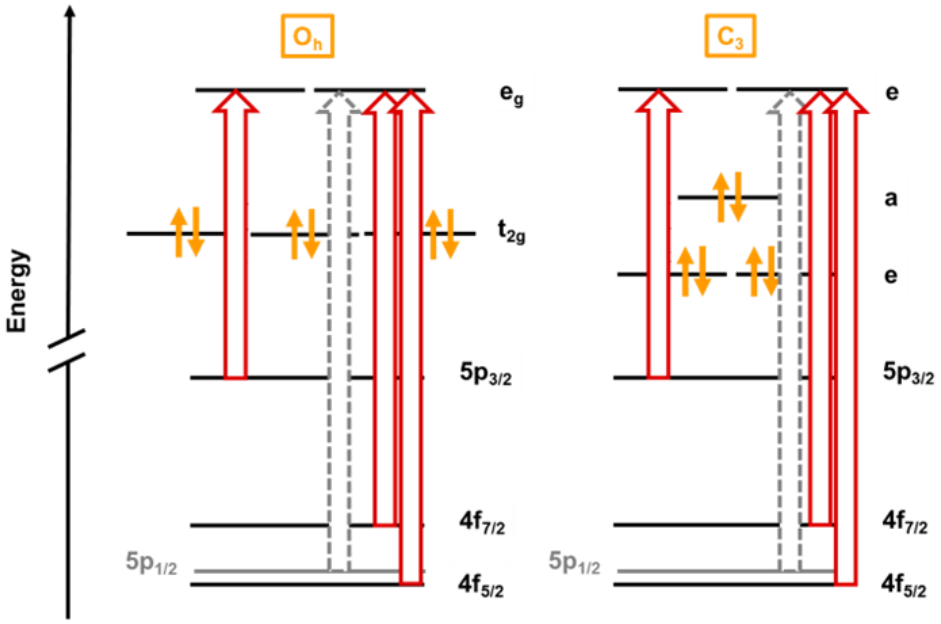

Figure S10. Simplified orbital manifold shown for an octahedral (A) or C_3-symmetric iridium(III) (d^6) center with allowed transitions as red arrows and unobserved $5p_{1/2}$ to valence trans in dotted grey arrows.

References

(1) Chang, H. T.; Guggenmos, A.; Chen, C. T.; Oh, J.; Géneaux, R.; Chuang, Y. De; Schwartzberg, A. M.; Aloni, S.; Neumark, D. M.; Leone, S. R. Coupled Valence Carrier and Core-Exciton Dynamics in WS_2 Probed by Few-Femtosecond Extreme Ultraviolet Transient Absorption Spectroscopy. *Phys. Rev. B* **2021**, *104* (6), 1–14. https://doi.org/10.1103/PhysRevB.104.064309.